Nanoscale

PAPER

View Article Online
View Journal | View Issue

Cite this: *Nanoscale*, 2026, **18**, 5884

A nanoscale view on oligo(ethylene glycol) self-assembled monolayer hydration

Nafiseh Samiseresht, Anne Jakubek, Petra Ebbinghaus and Martin Rabe *

Received 4th August 2025,
Accepted 6th February 2026

DOI: 10.1039/d5nr03300d

rsc.li/nanoscale

Self-assembled monolayers (SAMs) of oligoethylene glycol (OEG)-terminated thiols are often used in the design of protein-repellent interfaces. It is well known that their repellency depends on the crystallinity and conformation of the EG chains, and it is thought to be a consequence of interface water interacting with the OEG chains. Here, we provide novel insight into the structure and molecular conformation of OEG SAMs at a nanoscale level, focusing on the impact of immersion time (t_{im}) during preparation and relative humidity. Macroscopically, an increase in t_{im} leads to SAM densification and an increase in thickness, as well as a transition from amorphous OEG chains to predominantly helical crystalline chains. At the nanoscale, the morphology showed nano-domains of size dependent on t_{im}, and nano IR spectroscopy revealed direct spectroscopic evidence for different conformations prevalent in these domains. Hydration experiments conducted in an environment with increased humidity resulted in the nano-domains being hydrated to different extents. Water uptake led to an irreversible conformational transition of the helical domains. Additionally, nano IR spectroscopy demonstrated the absorbance of two differently hydrogen-bound water populations. These results shed new light on the nanophase behaviour of OEG SAMs and help to explain how nano-structure influences their protein repellency.

Introduction

Prevention of biofouling of surfaces and especially protein adsorption is a necessity in diverse applications. For example in surface-based diagnostic devices where the selective immobilization of proteins, cells, and biomolecules is key to the functionality, the prevention of non-specific adsorption is essential.[1–3] It is known that protein adsorption is influenced by both nano-scale surface chemistry and structure,[4,5] therefore self-assembled-monolayers (SAMs) of oligoethylene glycol (OEG) terminated thiols are frequently used to design protein repellent interfaces.[5–8]

Depending on the surface coverage and lateral packing density, the OEG chains can adopt different molecular conformations in the SAMs. For example, it was found that enforcing a high lateral density of the OEG molecules, *via* employing Ag substrates with small lattice spacing, leads to crystalline layers with EG chains in all-trans conformation.[5] In contrast, employing Au with larger lattice spacing allows EG chains to adopt helical, crystalline or amorphous conformations. The amorphous and helical conformation may also coexist leading to varying macroscopic crystallinities. Also, other factors such as chemical structure or the OEG length can influence the conformation. So it has for example been shown that an EG chain must have at least 5EG units to adopt a helical conformation.[9] While proteins readily adsorb on the all-trans OEG SAMs, helical OEG SAMs are protein repellent.[5]

The remarkable dependency of protein repellency on OEG conformation has been attributed to a preferential interaction of helical OEG chains with water and several experimental[10–13] and theoretical[14–17] studies confirmed strong interdependencies of molecular conformation and the OEG-water interactions. Surface force measurements even show long range repulsive forces on OEG-SAMs in the nanometer range and it was suggested that structured interface water may be the origin of this effect.[18–21]

Another aspect of SAM structure is the formation of nano-domains, which is an often observed phenomenon in SAMs in general[22–24] and in OEG containing SAMs in particular.[4,25–28] Spontaneous phase separation into nano domains can readily appear in mixed component systems due to thermodynamically driven unmixing at the interface,[22–26] but also in single component OEG SAMs nano domains with varying orientation and/or conformation have been reported.[4,27,28] For single component OEG SAMs the immersion time into the thiols solution during preparation has been identified as one parameter that controls both, formation of nano domains during growth[27] and the macroscopic crystallinity and conformation.[29–31] IR spectroscopy on OEG SAMs has been employed in these studies showing a general increased SAM

Department of Interface Chemistry and Surface Engineering, Max Planck Institute for Sustainable Materials, 40237 Düsseldorf, Germany. E-mail: m.rabe@mpi-susmat.de

helical crystallinity over time. However, the connection between nano-domain formation and macroscopic crystallinity and its impact on water adsorption has not been largely explored. Also, the influence of the OEG nano domains on the SAM functionality remains unknown.

In a recent study, we successfully employed nano-IR spectroscopy, namely AFM-IR, to study nano-phase separation in a mixed DNA-PEG SAM.[26] Here, we go a step further and use this method to resolve nano domains of varying molecular conformation in a single component EG_6OH SAM. The samples were prepared by controlling the immersion time t_{im} as a varying factor. Furthermore, we use AFM-IR to study the water sorption in the phase-separated SAM, its influence on the nano domain conformation and the local hydrogen bonding state of the adsorbed water.

Results and discussion

Macroscopic crystallinity correlates with nano domain abundance

Au(111)/OEG SAMs of 11-Mercaptoundecyl-hexa(ethylen glycol) (EG_6OH) with different surface coverage and crystallinity were prepared using the immersion time (t_{im}) as a varying factor. Infrared-reflection-absorption (IRRA) spectra recorded on OEG SAMs show vibrational bands expected for OEG SAMs (Fig. 1 and SI, Fig. S1).[5,19,32] The employed EG_6OH molecule consists of an alkyl and OEG segments, and the peak positions in the IRRA spectra may in principle give insight into the alkyl crystallinity and molecular conformation of OEG. The methylene vibrational modes of the two segments overlap, but an assignment to the respective molecule segments can be achieved by comparison with reference spectra.[5,32–35] In contrast, the ν(C–O) in (COC) can clearly be assigned to the OEG segment. Furthermore, specific effects arising due to the sampling method have to be considered. In IRRAS, the intensity of a vibrational peak depends on both the surface concentration and the orientation of a molecule. This orientation effect is explained by the surface selection rule for metals: absorption intensity is determined by the component of the transition dipole moment (TDM) perpendicular to the surface, while absorption from a TDM parallel to the surface is negligible.

In the following, specific marker bands are used that were assigned based on literature comparison (Table 1).[5,32–34] In particular theoretical studies have given insight into the conformation dependency of the IR spectra of OEG[33–35] and hence this assignment allows a direct conclusion of the OEG crystallinity. In the range from 900 cm^{-1} to 2000 cm^{-1}, the IRRA spectra recorded on Au(111)/OEG prepared from t_{im} = 2 minutes show a band at 1115 cm^{-1} assigned to ν(C–O) in helical crystalline OEG which appears together with two broader shoulders at the high frequency side (at *ca.* 1145 cm^{-1}). The appearance of this ν(C–O) shoulder indicates that a significant amount of amorphous OEG (Fig. 1a) coexists within the same monolayer. The long incubated (t_{im} = 24 hours) SAM shows a significantly narrower and more intense peak at 1115 cm^{-1}, whereas the high frequency shoulders appear less intense. This trend is well corroborated by normalized ν(C–O) spectra taken at intermediate timesteps

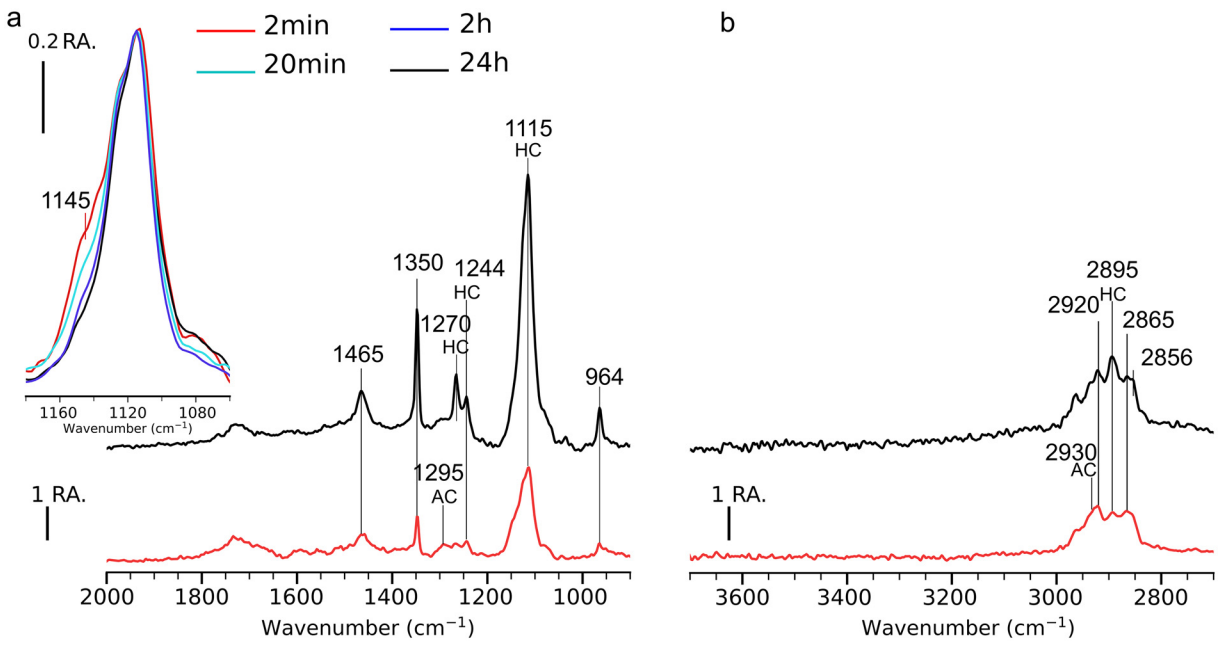

Fig. 1 IRRA spectra of Au(111)/OEG SAMs with different t_{im} as indicated by the legend. The markers in the spectra represent the peaks for amorphous conformation (AC) and helical conformation (HC) in the low (a) and the high wavenumber range (b). The inset represents the C–O–C bands normalized at 1115 cm^{-1}. Peak assignments are detailed in Table 1.

Table 1 Positions and assignments of vibrational modes for OEG SAMs in predominantly amorphous conformation, AC, and helical conformation, HC

Molecule segment	Mode assignments[5,33,34,36–38]		Mode position (cm^{-1})
Alkyl	$\delta(C–H_2)$		1465[a]
	$\nu_s(C–H_2)$		2856[a] (sh)
	$\nu_{as}(C–H_2)$		2920[a,b]
		HC	AC
OEG	$\rho(C–H_2)$	964[a]	964[a]
	$\nu(C–O–C)$	1115[a]	1115[a], 1145[a] (sh)
	$\tau(C–H_2)$	1244[a], 1270[a]	1295[a]
	$\omega(C–H_2)$	1350[a]	1350[a]
	$\delta(C–H_2)$	1465[a]	1465[a]
	$\nu_s(C–H_2)$	2890–2895[b], 2895[a]	2865[a,b]
	$\nu_{as}(C–H_2)$	2930[a] (sh)	2930[a] (sh), 2930[b] (s)

[a] Measured by IRRAS. [b] Measured by AFM-IR. Alkyl and OEG overlapping vibrations are discussed in the text; (sh: shoulder, s: strong).

that feature a continuous decrease of the 1145 cm^{-1} shoulder with respect to the maximum (Fig. 1a, inset).

The band at *ca.* 960 cm^{-1} is assigned to rocking $\rho(C–H_2)$, the bands at 1350 cm^{-1} and 1465 cm^{-1} are assigned to wagging $\omega(C–H_2)$ and scissoring $\delta(C–H_2)$ of OEG methylenes respectively. The intensity of these three bands increases with incubation time, probably due to an increase of the overall surface concentration at longer incubation. A series of shallow bands with centers at 1244 cm^{-1} and at *ca.* 1270 cm^{-1} are assigned to OEG associated twist $\tau(C–H_2)$ in perpendicular orientation to the helical axis, observed in a crystalline OEG, and the shoulder at *ca.* 1295 cm^{-1} is assigned to $\tau(C–H_2)$ observed in amorphous PEG.[5,34] In the IRRA spectra of shortly incubated OEG, these peaks show shallow intensity and broad bandwidths, which indicate OEG SAM's amorphous conformation. The peaks at 1244 cm^{-1} and 1270 cm^{-1} also increase upon increase of the incubation time to 24 hours. Based on the IRRAS spectra also the appearance of OEG all-trans conformations can be excluded because they would be expected to show a series of wagging modes around 1325 cm^{-1} and a single sharp C–O–C mode around 1145 cm^{-1}.[5,36]

Taken together in the lower wavenumber region, peak intensities generally increase with incubation time, which may be merely a result of an increase in surface concentration. However, other changes such as the narrowing of the $\nu(C–O)$ at 1115 cm^{-1} and the increase of the 1244 cm^{-1} to 1295 cm^{-1} ratio indicate a relative increase of the number of crystalline OEG segments with respect to amorphous segments. This becomes clearer from the analysis of the higher frequency range from 2700 cm^{-1} to 3700 cm^{-1}.

The alkyl segments of both short and long incubated SAMs absorb at 2856 cm^{-1} and 2920 cm^{-1}, assigned to symmetric and asymmetric methylene (ν_s, ν_{as})C–H_2 of the alkyl chains. Compared to fully-ordered aliphatic SAMs on gold with the bands at 2850 cm^{-1} and 2917 cm^{-1},[5,37] this indicates less ordered alkyl chains with *gauche* defects in the OEG SAM. The OEG segment absorbs at 2865 cm^{-1}, 2895 cm^{-1}, and 2930 cm^{-1} assigned to ν_s and $\nu_{as}(C–H_2)$ of amorphous or helical OEG as detailed in Table 1. With the increase of t_{im} most significantly the $\nu_s(CH_2)$ at 2895 cm^{-1} increases with respect to the neighboring alkyl bands. This band is characteristic of the helical-crystalline OEG[5,32,33] and hence its increase indicates that at longer incubation time, the ratio of crystalline OEG is significantly increased.

Further IRRAS measurements recorded on OEG SAMs prepared with t_{im} = 20 minutes and 2 hours support the observed trends (SI, Fig. S1). OEG SAMs formed with t_{im} = 2 hours and 24 hours especially show the peak at 2895 cm^{-1} characteristic for helical conformation with a stronger intensity. Hence, EG_6OH molecules in SAM adopt a higher ratio of crystalline helical conformations with increasing t_{im}, and already after t_{im} = 2 hours, a steady predominantly helical state is reached. The short ($t_{im} \leq 3$ minutes) incubated films and hence more amorphous SAMs are therefore in the following referred to as AC-SAMs, while the predominantly crystalline helical films ($t_{im} \geq 2$ hours) are termed HC-SAMs.

Additionally, spectroscopic ellipsometry (SE) measurements on OEG SAMs prepared from 2 min t_{im} and 24 hours were performed. The long incubated HC-SAM showed slightly but significantly lower Δ values than the shortly immersed AC-SAM (SI, Fig. S2). For thin films as studied here, a decrease in Δ represents an increase in the optical film thickness ($n \times d$). This means that both the SAMs refractive index (n) and thickness (d) may increase. Although a change in n, for example due to an increase in density, cannot be completely ruled out, we use a constant value for the quantitative analysis. A 3-layer optical model of [Au(111)|SAM (n = 1.45, d)| air (n = 1.0)], was used for fitting the measured spectroscopic $\Delta(\lambda)$ angles. The absolute thickness values show an average height of 2.85 nm ± 0.1 nm for AC-SAM and 3.1 nm ± 0.1 nm for HC-SAM (Fig. 2).

Atomic-force-microscopy (AFM) was employed to examine the morphological property of the OEG SAMs on the nanoscale. Tapping mode AFM topographies measured on AC-SAMs show formation of small islands separately distributed on the surface (Fig. 3a and b) in large and small scan areas. The islands have lateral dimensions of *ca.* 20 nm to 50 nm. AFM topographies measured on HC-SAM prepared with t_{im} = 2 hours, predominantly show a densely packed SAM resulting from the growth and coalescence of the islands (Fig. 3c and d) in large and small scan areas.

To further probe the structural variations governed by OEG molecules in the observed nano domains, nano IR spectroscopy (AFM-IR) was performed on AC SAMs. For this method, we achieved more precise measurements by employing a gold single crystal $Au(111)_{sc}$ substrate. Measuring on larger atomically smooth terraces eliminated the influence of imperfect substrate and enabled the identification of islands' borders with higher precision, as demonstrated by the tapping mode AFM topography on $Au(111)_{sc}$/OEG SAM in Fig. 4a and b. The elevated domains (islands) featured a height of approx. 3 nm, as depicted by the line scan (Fig. 4c).

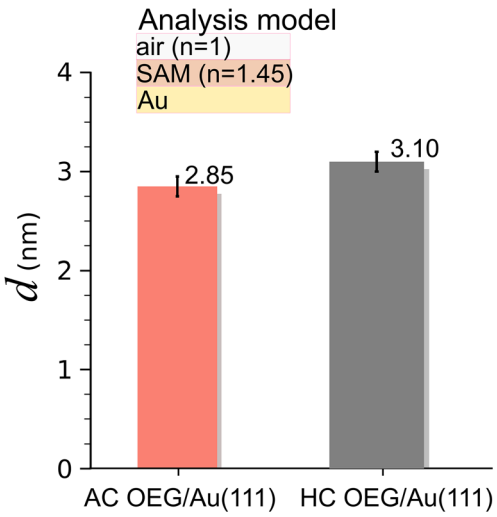

Fig. 2 Results of the thickness (d) determination from spectroscopic ellipsometry and for AC (t_{im} = 3 min) and HC (t_{im} = 24 h) SAM. Error bars represent the standard deviation from the average value recorded on SAMs + standard deviation in thickness of bare gold (0.02 nm causing sample-to-sample variation). Inset shows optical model used for analysis.

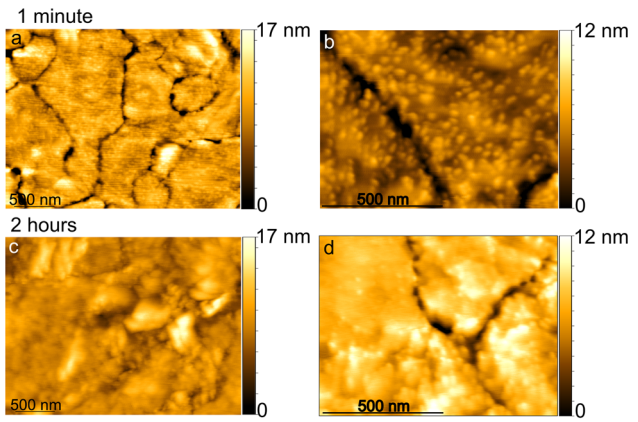

Fig. 3 Tapping mode AFM topography on OEG-SAMs on Au(111) from short and long immersion times t_{im}. Topography of OEG SAM prepared with: AC: t_{im} = 1 min (a and b) and HC: t_{im} = 2 hours (c and d) in large and small scan areas, respectively.

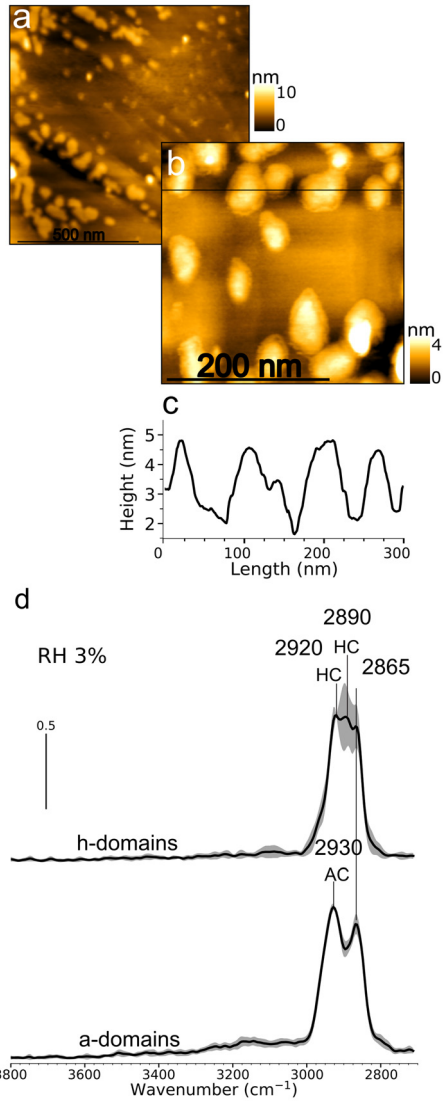

Fig. 4 Results of tapping mode AFM-IR measurements on AC Au(111)$_{sc}$/OEG SAM t_{im} = 3 min in dry atmosphere (RH 3%). Topography in large and small scan areas (a and b), line scan corresponding to the small scan (c), averaged nano-IR point spectra measured on h-domains (islands) and a-domains (low domains) (d) normalized at 2920 cm^{-1}. The shading represents the standard deviation of the spectrum averaged from measurements at 9 different positions.

Nano-IR point spectra were measured to examine the structure of OEG SAMs on elevated nano-domains and their surrounding. In general, it is noted that the spectral resolution of AFM-IR (10 cm^{-1}) is lower than the resolution in the IRRA spectra (4 cm^{-1}) discussed above. This leads to an overlap of close-by bands and apparent differences in the appearance of the AFM-IR *versus* IRRA spectra. Averaged nano-IR point spectra show clear ν(C–H$_2$) bands in the range 2800 cm^{-1} to 3000 cm^{-1} all over the sample, evidencing the presence of OEG molecules in both domain types and disproving the presence of uncovered Au interface. However, the spectra differ on the islands as compared to the spectra on the lower domains. Spectra show a band at 2865 cm^{-1}, both on islands and on the lower domains, that we assign to an overlap of alkyl and OEG ν_s(C–H$_2$) bands. The characteristic OEG HC band situated at 2890 cm^{-1} (ν_s(CH$_2$)) was clearly observed on the islands with its position varying between 2890 cm^{-1} to 2895 cm^{-1}, while it is absent on the low domains. A band at 2920 cm^{-1} appears on the island and is assigned to ν_{as}(CH$_2$) of alkyl segments. Its narrow bandwidth and high intensity bear a similarity to the IRRA spectra of long incubation time and high helical content. In contrast, the lower domains show a broader peak centered at 2930 cm^{-1} that we assign to overlapping ν_{as}(CH$_2$) of OEG and alkyl moieties showing an amorphous OEG conformation.

Taken together, averaged nano-IR point spectra show that OEG molecules predominantly take a crystalline helical conformation in the elevated domains, which are hence hereafter termed helical domains (h-domains). In contrast, the broadness of the bands, together with the absence of the OEG HC peak at 2890 cm^{-1}, indicates that the lower domains contain amorphous OEG chains, hence, they are termed amorphous domains (a-domains) hereafter.

To study the conformational distribution in a larger surface area with nanoscale lateral resolution, nano-IR mapping was performed at 2888 cm^{-1} to identify surface coverage of OEG h-domains. The direct comparison of tapping mode AFM topography (Fig. 5a) with the coincidentally recorded nano-IR map at 2888 cm^{-1} (Fig. 5b) on $Au(111)_{sc}$/OEG shows that the elevated domains have significantly higher IR-absorbance than the lower domains that showed no variations in the IR-map. Scans at larger scale gave similar results (SI, Fig. S3). Further separate nano-IR measurements probing the lower wavenumber region were performed on an OEG SAM with mainly h-domains present and yielded the expected OEG bands below 2000 cm^{-1}. (SI, Fig. S4). For further experiments under elevated humidity the higher wavenumber region is however of higher interest because it allows conclusions on both the OEG conformation *via* the $\nu_s(CH_2)$ and the H_2O content *via* the ν(OH) band as discussed below.

The data presented so far suggest the following picture for the studied system. Increasing the immersion time during OEG SAM formation leads to an increased surface coverage and an increase in the macroscopic helical-crystallinity observed by IRRAS. Tapping mode AFM revealed that this increase is accompanied by an increase in the surface area covered by elevated nano-domains. AFM-IR results indicated that these elevated nano-domains have a high degree of helicity (h-domains), whereas the low domains contain amorphous OEG chains (a-domains). It is well accepted that the formation of SAM films proceeds *via* island growth and coalescence.[39,40] Also, nano-gaps that have been observed in full-grown OEG monolayers[28] may be a remnant of the island coalescence. An ideal OEG SAM with the all-trans alkyl-chains tilted by 30 degree from the normal and capped by helical OEG is expected to be about 3.08 nm thick.[5] This theoretical value is in good agreement with the thickness of long-incubated OEG SAM obtained from modeling the SE data. The reduced optical thickness of shortly incubated films does not contradict the picture of a patchy film with growing islands. In SE, the optical thickness is also expected to be lowered in a layer model with islands compared to a homogeneous layer model. The height difference between islands and their surrounding measured from the AFM topography was about 3 nm, *i.e.* also very close to the ideal OEG SAM thickness. However, AFM-IR provides direct spectroscopic evidence that the a-domains are covered with amorphous OEG SAM. Hence, it is assumed that the molecules in the low domains must be lying flat on the substrate to explain the observed height difference. The island growth is understood as an uprising of molecules from the lying down phase due to a densification of the material in the a-domains.

Next, we studied the observed nano domains under elevated relative humidity to learn about structural changes caused by water adsorption.

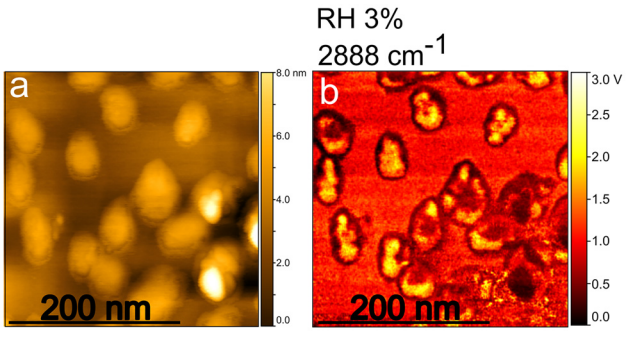

Fig. 5 Results of tapping mode AFM-IR on AC $Au(111)_{sc}$/OEG t_{im} = 3 min in dry (RH 3%) environment; topography (a), nano IR-mapping at maximum of $\nu_s(C-H_2)$ 2888 cm^{-1} (b).

Water adsorption depends on nano domain coverage

Spectroscopic ellipsometry on OEG AC-SAM and OEG HC-SAM was measured *in situ* under controlled increments of relative humidity (RH%) to investigate the thickness variation upon hydration of the SAMs under study here. The thickness change of the hydrated SAMs with respect to the unhydrated SAM was determined from fitting the averaged measured Δ values to a 3-layer optical model of [Au + dry SAM (n_{ref})|SAM thickness change (n = 1.45, δd)|air (n = 1.0)]. Here Au + SAM (dry) stands for the respective SAM at the beginning of the experiment under dry conditions and n_{ref} was obtained by point-wise inversion of the respective Δ and Ψ angles. The thickness increase δd obtained in this way is under the assumption of constant humidity independent SAM refractive index (n = 1.45) and is independent of variations of the substrate optical properties (Fig. 6). With increasing water activity from 50 to 94 RH%, the AC-SAM shows thickness increase (δd) from about 1 Å at *ca.* RH = 50% to about 6 Å at *ca.* RH = 94%. In contrast, the SE thickness measurements on HC-SAM show no measurable height variations until a 1 Å elevation in thickness at RH = 86%. Then, the thickness continuously increases and reaches a much lower maximum of 2 Å at RH 96%.

The SE thickness measurements on the hydrated SAM indicate that the OEG AC-SAM starts a subtle swelling at exposure to RH 50%, followed by a stronger swelling above 70%, whereas the OEG HC-SAM swells only at relative humidities above RH 80%. OEG AC-SAM shows much higher thickness increase than OEG HC-SAM, and at very high RH, the increase in hydrated AC-SAM is about 4 Å higher than hydrated HC-SAM.

Two separate processes might be expected to occur upon humidity increase, either separately or coincidentally. Firstly, water may penetrate into the hydrophilic EG segments as suggested for various OEG films by IR,[10,11] SFG[12,13] and theoretical studies[16,17,41] Secondly, a thin water film on the SAM may

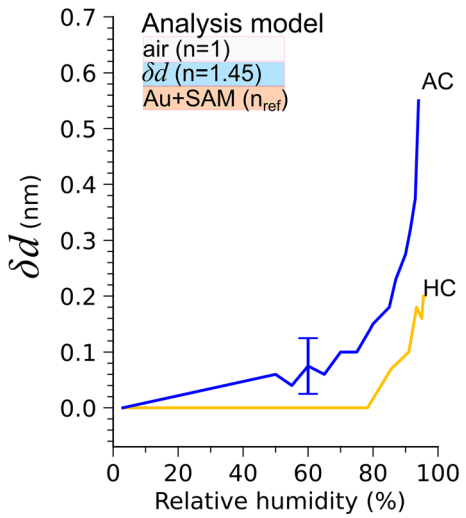

Fig. 6 Results of the thickness measurements by SE. The thickness change (δd) of OEG AC and OEG HC SAMs t_{im} = 3 min and t_{im} = 24 h upon increase in RH%. Inset shows optical model used for analysis. Error bar represents the maximum typical sample-to-sample deviation for these measurements, determined from the difference in thickness recorded on different AC SAMs at RH 60%.

form as for instance observed on the Au solid interface (SI, Fig. S5) and other impenetrable solid materials,[42] as well as highly ordered and hence impermeable SAMs of alkylthiols.[43,44] At low water activities (RH) such films may even feature submonolayer coverage.[45] For both effects, a similar effect on Δ would be expected in ellipsometric measurements. For the analysis we chose a model of constant refractive index and a variation of layer thickness as this most closely reflects the penetration model supported by most literature sources on OEG SAMs. Nevertheless, an additional water adsorption on top of the SAM cannot be fully excluded.

Helical OEG segments have been shown experimentally[10–13] and theoretically[16,17,41] to significantly alter their conformation upon water penetration. For instance, by means of PM-IRRAS Skoda *et al.* observed a red shift of the ν(C–O–C) band upon hydration of EG_3 SAMs.[10] Furthermore, the red shift increased with decreasing OEG coverage, indicating an increased penetration upon lower coverage. Vanderah *et al.* found indications for an increased water penetration into amorphous OEG SAMs by impedance measurements.[11] Also, for highly ordered EG_5 films penetration was observed while highly ordered EG_6 films showed lower penetration. After longer incubation, slow water penetration of the EG_6 films was observed as well. Theoretical work suggests that short EG_3 SAMs elongate substantially taking in configurations that resemble the all-trans state.[17] For the SAM studied here, the expected film thickness increase for a variation from upright helical to upright all-trans configuration would be about 0.47 nm.[5] The simple analysis model in Fig. 6 results in a smaller thickness change upon hydration of HC-SAM. Hence, if water penetration occurs in this system the overall perturbation of the OEG does probably not result in fully upright extended configuration of OEG chains. Amorphous OEG chains in contrast, feature an increased portion of conformers with *gauche* dihedral angles along the C–O bonds from the start. Here, the elongation reachable from *gauche–trans* transitions upon hydration is expected to be bigger which is in line with the observed stronger thickness increase of AC-SAM. Furthermore, in the less dense domains an additional effect might be an orientational uprise of molecules that is expected to be represented in the measured thickness. Of course it must be considered that as shown by AFM-IR above, the studied AC-SAM consists of nano domains of helical OEG surrounded by amorphous segments and hence the observed thickness increase must be understood as the weighted average of the thickness increase due to swelling in the two different nano phases.

Conformational changes in hydrated OEG nano domains

To understand the impact of water uptake on the SAM nano structures, nano-IR point spectra on hydrated $Au(111)_{sc}$/OEG AC-SAM were measured under varying RH% between 3% to 95%. The nano-IR point spectra recorded on h- and a-domains displayed in Fig. 7 were normalized at the maximum of the common peak and for the following discussions of peak intensities it has to be kept in mind that intensities are referred to this band. After measurements in the dry discussed above a

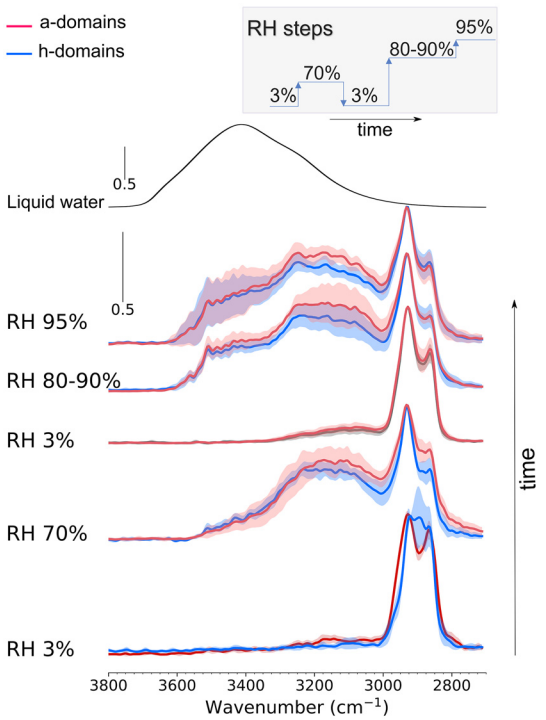

Fig. 7 Results of averaged nano-IR point spectra recorded on Au $(111)_{sc}$/OEG (AC, t_{im} = 3 min) amorphous conformation domains, a-domains (red tones) overlay on helical conformation domains, h-domains (blue tones) at varying RH%. The shading represents the standard deviation from the averaged spectrum. Inset depicts RH variation program.

first increase of the relative humidity to 70% was applied for 16 hours. Nano-IR point spectra on $Au(111)_{sc}$/OEG h-domains and a-domains show that the appearance of broad water related ν(OH) stretching bands centered at 3200 cm^{-1} is accompanied by significant variations in the ν(CH) bands from 2800 cm^{-1} to 3000 cm^{-1}. This observations clearly indicates that water penetrates the hydrophilic OEG part of the SAM and alters the OEG conformation. The two main maxima of the a-domains shift from *ca.* 2920 cm^{-1} to 2932 cm^{-1} and from *ca.* 2868 cm^{-1} to 2865 cm^{-1}. Furthermore, the high frequency band appears less broad upon the first humidity increase, while the low frequency mode loses significant intensity with respect to the high frequency mode (*i.e.* peak ratio ν_l/ν_h decreases). On the other side the h-domains feature a prominent loss of the helical OEG peak at 2890 cm^{-1} upon the first humidity increase. The 70% spectrum of h-domains features significant similarities to the respective a-domain spectrum except for a slightly increased peak ratio ν_l/ν_h.

It is evident that structural changes occur for both a- and h-domains upon hydration. However, compared to the IRRA spectra the bands in the nano-IR spectra appear broader and the OEG- and alkyl-related bands cannot be unequivocally resolved underneath the broad spectral envelopes, except for the helical OEG peak at 2890 cm^{-1}. This may be due to the lower spectral resolution in the AFM-IR spectra. Nevertheless, the two main observations are 1: the loss of helicity in h-domains indicated by the disappearance of the 2890 cm^{-1} band and 2: the significant reduction of the ν_l/ν_h intensity ratio for both a- and h-domains. Also in AFM-IR orientational effects are expected to influence relative peak intensities due to the selection rules on metals. Hence, the ν_l/ν_h intensity ratio variation implies an orientational and/or conformational change. Spectra with higher frequency resolution as well as simulations would be necessary to more precisely determine the nature of this structural variation.

In the experiment, next a drying step was exerted by reducing the RH back to 3% (Fig. 7) for 72 hours. The almost complete disappearance of the ν(OH) stretching band at 3200 cm^{-1} shows that water could be effectively desorbed from the SAM. The changes within the CH stretching region however where found to be only partially reversible and a- and h-domains show effectively equal spectra after this drying step. The peak positions are slightly shifted back to 2928 cm^{-1} and 2864 cm^{-1}. Also the ν_l/ν_h intensity ratio is slightly increased upon dehydration. Obviously, the initial crystalline helical state of the h-domains is not recovered upon dehydration within the time frame of the experiment (drying in 3% RH for 72 hours).

Finally, a further re-hydration to higher RH above 80% was exerted resulting in another blue shift of the peak positions back to 2932 cm^{-1} and to 2865 cm^{-1} and again a reduction of nu_l/nu_h intensity ratios. In these rehydrated states the nano IR spectra of a- and h-domains appear indistinguishable in the CH stretching region, which indicates a high structural similarity between the hydrated SAMs. In the re-hydration step no significant differences were observed in the spectra at 95% as compared to the spectra in the range 80% to 90%.

Absorbed water is strongly hydrogen bound

The averaged spectra after the first hydration at 70% for both a-domains and h-domains show a broad ν(OH) from 3000 cm^{-1} to 3575 cm^{-1} with the maximum at 3200 cm^{-1} (Fig. 7). The ν(OH) band was mostly removed after the SAM was dried by purging the environmental chamber with a constant flow of dry nitrogen for *ca.* 3 days. However, a minor ν(OH) component remained in the spectrum centered at 3100 cm^{-1}. After another rehydration by exposure to RH 80% both a- and h-domain spectra show a broad ν(OH) absorption with two distinguishable components, the stronger band ranges from 3000 cm^{-1} to 3330 cm^{-1} with a maximum at *ca.* 3200 cm^{-1} (Fig. 7), similar to the OH band that appeared in spectra at the first hydration at RH 70%. The second, lower intensity component is in the range from 3330 cm^{-1} to 3600 cm^{-1} with a maximum at *ca.* 3400 cm^{-1}. The further increase to about 95% relative humidity did not change the OH spectra significantly. The direct comparison of the nano IR spectra shows that a-domains in hydrated states (70%, 80%, 95%, Fig. 7) have constantly higher intensity of the 3200 cm^{-1} OH component as compared to the h-domains. This correlation is also corroborated by nano-IR imaging experiments.

The direct comparison of nano-IR images recorded at the OH stretching band maxima at 3% with images recorded at 70% reveals a significantly increased contrast between a- and h-domains at higher humidity (Fig. 8). The h-domains clearly feature a lower OH intensity and hence water amount.

The complex shapes of IR water OH-stretching bands result from an intricate interplay of processes in which intra- and intermolecular coupling of normal modes and hydrogen bonding play key roles. Thus, a direct assignment of the components of the broad OH band of liquid water to populations of molecules remains a matter of debate.[46–49] Nevertheless, it is generally accepted that the OH band position of water is substantially influenced by the hydrogen bonding environment, causing a red-shift with increasing H-bond strength. Comparing the spectral shape of our nano IR OH spectra with a spectrum of bulk water hence gives insight about changes of waters' hydrogen bond network upon absorption.

The OH band observed after the first absorption step has a maximum around 3230 cm^{-1} (RH above 70%) and the com-

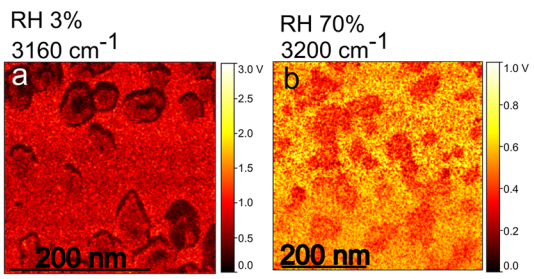

Fig. 8 Results of tapping mode AFM-IR on $Au(111)_{sc}$/OEG (AC, t_{im} = 3 min). Comparison of IR mappings of maximum of ν(OH) in dry at 3160 cm^{-1} (a) and in humid environment at 3200 cm^{-1} (b).

parison with the bulk water spectrum[50] shows that the absorbed water is significantly stronger hydrogen-bonded than bulk water molecules (Fig. 7).

After drying the SAM in a nitrogen environment, a broad OH band remains with small intensity, representing residual water that was not removable by nitrogen flow. The bands position at low frequency from 3030 cm^{-1} to 3200 cm^{-1} indicates that this residual water is strongly H-bonded.

After rehydration the ν(OH) stretching components show higher intensities in the spectra at 80% to 90% and at 95% than in the spectra at RH 70%. This indicates that an increase in humidity promotes further water absorption. Furthermore, the spectra show an increased intensity at higher wavenumbers (centered at 3370 cm^{-1}) as compared to the 70% spectra. This indicates the presence of a second component that we assign to an additional second species of water with a different, namely less strong bound hydrogen-bond environment as compared to the initially absorbed water. In comparison to bulk water this water type features comparable H-bonds as concluded from the spectral comparison (Fig. 7). However it must be noted, that due to the sample history in the reported experiment it cannot be fully excluded that the observed differences at higher humidity are also in part influenced by the intermediate dehydration step. Further experiments are necessary to clarify this. For the qualitative interpretation of the results the sample history thus needs to be kept in mind.

The analysis of the humidity dependent nano IR spectra reveals an inhomogeneous water adsorption that is caused by the structural differences in the nano-domains of the studied system. We consider the observed differences in the crystallinity in a- and h-domains to arise from the different molecule density in these domains. Water penetration into the SAMs nano domains in the first hydration step led to strongly H-bound water that we assign to water molecules H-bonding directly to ether moieties of OEG. The adsorbed water leads to significant irreversible loss of helicity in the h-domains and to more equal OEG structures in a- and h-domains. As discussed on base of the SE results the structural change and loss of helicity upon water absorption have been found before in theoretical and experimental studies and nano-IR spectra show that these processes occur locally on the nanoscale in the heterogenous films studied here. Despite the structural variation, upon hydration the molecular density differences between the nano domains must prevail since the thiols are covalently bound to the gold interface. This reasoning helps to understand the conclusion from ν(OH) nano-IR images and the analysis of the OH band shape which showed that a-domains contain more ether H-bound water than h-domains whereas the amount of the second, less strongly H-bound water type was comparable amongst the domains. A possible explanation for this observation is a deeper penetration of water molecules into the OEG SAM. This is in line with theoretical studies which predict both strong H-bonds between water and C–O–C and an increased water penetration for less dense OEG-terminated SAMs.[31,41] We attribute the second water species to molecules in between the OEG chains but not directly H-bound to the ether moiety which explains why it appears more bulk like, judged on basis of its OH band position.

Summary and conclusion

This work highlights the importance of nano domain formation for the macroscopic properties and functionally of SAMs. The macroscopic crystallinity and density of Au(111)/OEG nanostructured SAMs prepared from solution was varied by controlling the immersion time. OEG SAM showed higher proportion of crystalline-helical conformation (HC) as well as increased thickness with increasing t_{im}. AFM-IR provided evidence that the increase of crystallinity is related to growth of high density, helical crystalline domains that are surrounded by low density domains with amorphous OEG chains. The h-domains with upright conformation were formed within the initial minutes of SAM formation. Control of the immersion times allowed control over the size and distribution of h-domains. Under elevated relative humidity, the lower a-domains uptake higher amounts of water that is strongly H-bonded to the C–O–C groups of OEG. The h-domains on the other side irreversibly lose helical order upon water sorption resulting in similar OEG structures for hydrated a- and h-domains. The density and conformation of OEG chains as well as their water sorption properties have been identified as key factors for the protein repellent character of OEG SAMs. Our work implies that nano domain formation of protein repellent SAMs can lead to local variations of these properties and hence is another important factor that determines the macroscopic anti-fouling properties of surfaces.

Materials and methods

Materials

Gold single crystal with predominantly (111) orientation (Mateck GmbH, Germany) and commercially available polycrystalline, evaporated gold (250 nm) on glass (Arrandee metal GmbH + Co. KG, Germany) were employed as substrates. 11-Mercaptoundecyl-hexa(ethylen glycol) (OEG) $HS(CH_2)_{11}(OCH_2CH_2)_6OH$ (Sigma-Aldrich, Germany) was used for SAM immobilization. 1-Octadecane-d37-thiol $ODTD_{37}$ (CDN ISOTOPES GmbH, Germany) was used for IRRAS reference SAMs. Ultra-pure water with 18.2 MΩ cm resistivity (ELGA LabWater) for rinsing and absolute ethanol 99.9% (Merck, Germany) for dilution and rinsing were used. Nitrogen and argon used throughout this work was of grade 5.0 purity.

Sample preparation

The OEG monolayers were immobilized on an ultra-flat Au (111) surface. The polycrystalline Au(111) or single crystal Au $(111)_{sc}$ was hydrogen flame annealed for 3 to 10 minutes and cooled in a nitrogen stream before immersion in the OEG thiol solution. The Au(111) were immersed in argon-saturated solution of OEG in ethanol with low 10 μM and high 15 μM to

20 μM concentrations. Immersion times of $t_{im} \leq 3$ minutes and 20 minutes, 2 hours, and 24 hours were used to achieve high and low packing densities of OEG monolayers. The OEG monolayers were rinsed with absolute ethanol and dried in a nitrogen stream. The background sample for IRRAS was prepared by immersing Au(111) in argon-saturated solution of 0.1 mM $ODTD_{37}$ in ethanol overnight. The sample was subsequently, rinsed with absolute ethanol and ultra-pure water and dried in a nitrogen stream.

Infrared-reflection-absorption spectroscopy, IRRAS

A VERTEX 70v FT-IR spectrometer equipped with a high power Mid-IR globar light source and a mercury-cadmium-telluride (MCT) detector was employed for measurements in the spectral range from 900 cm^{-1} to 4000 cm^{-1}. The beam traversed a standard KBr beam splitter and a sample compartment with glass windows. The measurements were done in vacuum using an external reflection unit (Seagull, Harrick Scientific Products, Inc., New York) set at p-polarization and at an incident angle of 80°. An approx. area of 30 mm^2 of sample was exposed to the incident beam. The spectra were obtained at 4 cm^{-1} resolution with 1024 scans accumulation per spectrum.

Spectroscopic ellipsometry, SE

A spectroscopic ellipsometer SE 800 (SENTECH instrument GmbH, Germany) with SpectraRay/4 software was employed. The spectra were recorded in a custom built, enclosed Teflon cell with beam inlet at the angle of 70°. An approx. area of 3 mm^2 of sample was exposed to the incident beam. The spectroscopic Δ angles were recorded in dry for Au(111) and Au(111)/OEG and in selected relative humidity, RH%. The RH was established to a desired percentage by mixing dry and water-saturated nitrogen streams. The water-saturated nitrogen flow was obtained by passing the nitrogen stream through a bottle of deionized water gas bubblers, including DI water, in a thermostat water bath set at a fixed temperature. The humidity was measured by means of a SHT71 sensor (Sensirion AG, Switzerland), placed within the cell approx. 1 cm above the sample. Care was taken to prevent condensation in the sample chamber by slow manual ramping procedures over several hours to prevent overshooting. Overshooting might be an issue at high RH% values leading to condensation on the cell windows or sample and hence unusable data. Spectra were recorded at constant time intervals of 15 min to 30 min. A 3-layer model [Au(111) |SAM (n = 1.45, d)| air (n = 1.0)] was used to determine the SAM thickness d by fitting the measured Δ spectra in the range from 550 nm to 830 nm where the Au(111)/OEG was found transparent. The dispersion of Au(111) optical constants was calculated by point-wise inversion of one set of experimentally measured (Δ, Ψ) angles and used in the model. The SAM layer was assumed to have a wavelength-independent refractive index (n = 1.45), and the ambient layer was considered air (n = 1). In thickness measurements for SAMs in dry environment to consider for the error caused by variation of Au(111) optical constants from sample to sample the 3-layer model was applied to several Au(111) samples and an averaged thickness of 0.03 nm ± 0.02 nm was calculated from 5 measurements. This value was subtracted from the SAMs thickness, including the standard deviation in the error bars. The resulting thicknesses were averaged over 3–5 positions on SAM samples.

The measurements in humid environment were at the same point on the sample with thickness (δd_0). In order to exclude the influence of variation of Au dispersion from sample to sample, the dispersion was calculated by point-wise inversion of from a set of (Δ, Ψ) angles measured on Au(111)/OEG in a dry environment. The thickness variations were determined by fitting a 3-layer model [Au + dry SAM (n_{ref})|SAM thickness change (n = 1.45, δd)|air (n = 1.0)]. Here Au + SAM (dry) stands for the respective SAM at the beginning of the experiment under dry conditions. The δd determined in a humid environment show qualitatively the same behavior as if the pure Au dispersion was employed in the model, although this approach would have let to higher errors. The error bars for thickness change in humid environments represent the maximum sample-to-sample variation of thickness on two hydrated AC SAMs (0.05 nm at RH 60%) and on two Au samples exposed to RH% (0.06 nm at RH 80%).

Nano-IR spectroscopy, AFM-IR

A Nano-IR 3 (Bruker Corporation, USA) equipped with an enclosed, custom built environmental chamber and two mid-IR tunable laser sources was employed. Quantum Cascade Lasers (QCL, MIRcat, DRS Daylight Solutions) covering 905 cm^{-1} to 1970 cm^{-1} and a fast Optical parametric oscillator (OPO, firefly laser, M Squared Lasers Inc.) covering 2700 cm^{-1} to 3800 cm^{-1} were used. The topography, IR-mapping, and point spectra were recorded in tapping mode AFM-IR using a gold-coated silicon tip with a nominal fundamental resonance frequency of 75 kHz ± 15 kHz and a nominal tip radius of ≤25 nm(Tapping Mode NIR2 Probes, PR-EX-TnIR-A-10, Bruker AFM probes, USA). The phase-locked loop (PLL) was enabled during nano-IR mapping to track the frequency and keep it aligned with the repetition rate of OPO *ca.* 189 kHz and QCL *ca.* 350 kHz tuned at a specific wavenumber. The laser powers were optimised for the OPO laser in the range 0.5 mW to 0.9 mW and for the QCL laser in the range 0.3 mW to 1.6 mW to obtain a good signal to noise ratio. Images were recorded with 256 × 256 pixels and scan rate of 0.5 Hz to 1 Hz. The point spectra were analyzed after a minimal 3-point smoothing routine applied by Analysis Studio software. The spectra were normalized at a peak maximum to account for the impact of tip geometry and substrate topography, as well as measurement conditions like laser power and RH%. The relative humidity was controlled by purging a mixture of dry and water-saturated nitrogen flow *via* isolated tubings into the environmental chamber, by means of an automated RH generator (RH-200, L&C Science and Technologies, USA). An increase in RH turbulences in the environment aggravates drifts in AFM imaging; therefore, the measurements were done after proper waiting times of at least 12 hours to reach optimum equilibrium after change of the RH. The humidity

was measured by a SHT31-ARP-B sensor (Sensirion AG, Switzerland) inserted in the environmental chamber close to the sample. Care was taken to prevent condensation in the sample chamber by slow ramping procedures to prevent overshooting. Nano-IR point spectra were recorded in dry nitrogen environment and under step-wise continuous exposure to RH 70%, 80%, and 95%.

Author contributions

Conceptualization, supervision, and funding acquisition: M. R.; formal analysis: N. S. and M. R.; visualisation and writing – original draft: N. S.; investigation and writing – review & editing: all authors.

Conflicts of interest

There are no conflicts to declare.

Data availability

The raw data of the published material is available *via* the Edmond Repository at: https://doi.org/10.17617/3.ENIDUF

Supplementary information: additional IRRAS data on Au (111)/OEG SAMs prepared from different immersion times, averaged $\Delta(\lambda)$ spectra recorded on HC and AC SAMs, additional AFM-IR spectroscopy and imaging data also in the fingerprint region, and SE results on water film thickness adsorbed on Au (111) at varying RH%. See DOI: https://doi.org/10.1039/d5nr03300d.

Acknowledgements

This work is funded by the Deutsche Forschungsgemeinschaft (DFG, German Research Foundation) under Germany's Excellence Strategy – EXC 2033 – 390677874 - RESOLV. Open Access funding provided by the Max Planck Society.

References

1 S. Zhang, R. Geryak, J. Geldmeier, S. Kim and V. V. Tsukruk, Synthesis, Assembly, and Applications of Hybrid Nanostructures for Biosensing, *Chem. Rev.*, 2017, **117**, 12942–13038.

2 F. V. Oberhaus, D. Frense and D. Beckmann, Immobilization Techniques for Aptamers on Gold Electrodes for the Electrochemical Detection of Proteins: A Review, *Biosensors*, 2020, **10**, 45.

3 M. Frasconi, F. Mazzei and T. Ferri, Protein immobilization at gold–thiol surfaces and potential for biosensing, *Anal. Bioanal. Chem.*, 2010, **398**, 1545–1564.

4 L. Li, S. Chen and S. Jiang, Protein Adsorption on Alkanethiolate Self-Assembled Monolayers: Nanoscale Surface Structural and Chemical Effects, *Langmuir*, 2003, **19**, 2974–2982.

5 P. Harder, M. Grunze, R. Dahint, G. M. Whitesides and P. E. Laibinis, Molecular Conformation in Oligo(ethylene glycol)-Terminated Self-Assembled Monolayers on Gold and Silver Surfaces Determines Their Ability To Resist Protein Adsorption, *J. Phys. Chem. B*, 1998, **102**, 426–436.

6 K. L. Prime and G. M. Whitesides, Self-Assembled Organic Monolayers: Model Systems for Studying Adsorption of Proteins at Surfaces, *Science*, 1991, **252**, 1164–1167.

7 K. L. Prime and G. M. Whitesides, Adsorption of proteins onto surfaces containing end-attached oligo(ethylene oxide): a model system using self-assembled monolayers, *J. Am. Chem. Soc.*, 1993, **115**, 10714–10721.

8 H. Vaisocherová, E. Brynda and J. Homola, Functionalizable low-fouling coatings for label-free biosensing in complex biological media: advances and applications, *Anal. Bioanal. Chem.*, 2015, **407**, 3927–3953.

9 D. J. Vanderah, J. Arsenault, H. La, V. Silin, C. W. Meuse and R. S. Gates, Helical, Disordered, and What that Means: Structural Characterization of a New Series of Methyl 1-Thiaoligo(ethylene Oxide) Self-Assembled Monolayers, *MRS Proc.*, 2002, **724**, N4.5.

10 M. W. A. Skoda, R. M. J. Jacobs, J. Willis and F. Schreiber, Hydration of Oligo(ethylene glycol) Self-Assembled Monolayers Studied Using Polarization Modulation Infrared Spectroscopy, *Langmuir*, 2006, **23**, 970–974.

11 D. J. Vanderah, J. Arsenault, H. La, R. S. Gates, V. Silin, C. W. Meuse and G. Valincius, Structural Variations and Ordering Conditions for the Self-Assembled Monolayers of $HS(CH_2CH_2O)3\text{-}6CH_3$, *Langmuir*, 2003, **19**, 3752–3756.

12 M. Zolk, F. Eisert, J. Pipper, S. Herrwerth, W. Eck, M. Buck and M. Grunze, Solvation of Oligo(ethylene glycol)-Terminated Self-Assembled Monolayers Studied by Vibrational Sum Frequency Spectroscopy, *Langmuir*, 2000, **16**, 5849–5852.

13 R. Y. Wang, M. Himmelhaus, J. Fick, S. Herrwerth, W. Eck and M. Grunze, Interaction of self-assembled monolayers of oligo(ethylene glycol)-terminated alkanethiols with water studied by vibrational sum-frequency generation, *J. Chem. Phys.*, 2005, **122**, 164702.

14 R. L. C. Wang, H. J. Kreuzer and M. Grunze, Molecular Conformation and Solvation of Oligo(ethylene glycol)-Terminated Self-Assembled Monolayers and Their Resistance to Protein Adsorption, *J. Phys. Chem. B*, 1997, **101**, 9767–9773.

15 A. J. Pertsin, M. Grunze and I. A. Garbuzova, Low-Energy Configurations of Methoxy Triethylene Glycol Terminated Alkanethiol Self-Assembled Monolayers and Their Relevance to Protein Adsorption, *J. Phys. Chem. B*, 1998, **102**, 4918–4926.

16 A. J. Pertsin and M. Grunze, Computer Simulation of Water near the Surface of Oligo(ethylene glycol)-Terminated Alkanethiol Self-Assembled Monolayers, *Langmuir*, 2000, **16**, 8829–8841.

17 A. J. Pertsin, T. Hayashi and M. Grunze, Grand Canonical Monte Carlo Simulations of the Hydration Interaction between Oligo(ethylene glycol)-Terminated Alkanethiol Self-Assembled Monolayers, *J. Phys. Chem. B*, 2002, **106**, 12274–12281.

18 T. Hayashi, Y. Tanaka, Y. Koide, M. Tanaka and M. Hara, Mechanism underlying bioinertness of self-assembled monolayers of oligo(ethyleneglycol)-terminated alkanethiols on gold: protein adsorption, platelet adhesion, and surface forces, *Phys. Chem. Chem. Phys.*, 2012, **14**, 10196.

19 T. Sekine, S. Asatyas, C. Sato, S. Morita, M. Tanaka and T. Hayashi, Surface force and vibrational spectroscopic analyses of interfacial water molecules in the vicinity of methoxy-tri(ethylene glycol)-terminated monolayers: mechanisms underlying the effect of lateral packing density on bioinertness, *J. Biomater. Sci., Polym. Ed.*, 2017, **28**, 1231–1243.

20 M. Tanaka, S. Kobayashi, D. Murakami, F. Aratsu, A. Kashiwazaki, T. Hoshiba and K. Fukushima, Design of Polymeric Biomaterials: The "Intermediate Water Concept", *Bull. Chem. Soc. Jpn.*, 2019, **92**, 2043–2057.

21 M. Tanaka, S. Morita and T. Hayashi, Role of interfacial water in determining the interactions of proteins and cells with hydrated materials, *Colloids Surf., B*, 2021, **198**, 111449.

22 L. J. Jeuken, N. N. Daskalakis, X. Han, K. Sheikh, A. Erbe, R. J. Bushby and S. D. Evans, Phase separation in mixed self-assembled monolayers and its effect on biomimetic membranes, *Sens. Actuators, B*, 2007, **124**, 501–509.

23 S. Chen, L. Li, C. L. Boozer and S. Jiang, Controlled Chemical and Structural Properties of Mixed Self-Assembled Monolayers by Coadsorption of Symmetric and Asymmetric Disulfides on Au(111), *J. Phys. Chem. B*, 2001, **105**, 2975–2980.

24 Q. Ong, N. Nianias and F. Stellacci, A review of molecular phase separation in binary self-assembled monolayers of thiols on gold surfaces, *Europhys. Lett.*, 2017, **119**, 66001.

25 G. Figueroa-Miranda, C. Wu, Y. Zhang, L. Nörbel, Y. Lo, J. A. Tanner, L. Elling, A. Offenhäusser and D. Mayer, Polyethylene glycol-mediated blocking and monolayer morphology of an electrochemical aptasensor for malaria biomarker detection in human serum, *Bioelectrochemistry*, 2020, 107589.

26 N. Samiseresht, G. Figueroa Miranda, A. Das, K. Graef, D. Mayer and M. Rabe, Nano-Phase Separation and Analyte Binding in Aptasensors Investigated by Nano-IR Spectroscopy, *Small*, 2025, 2409369.

27 J. Rundqvist, J. H. Hoh and D. B. Haviland, Poly(ethylene glycol) Self-Assembled Monolayer Island Growth, *Langmuir*, 2005, **21**, 2981–2987.

28 N. Inada, H. Asakawa, Y. Matsumoto and T. Fukuma, Molecular-scale surface structures of oligo(ethylene glycol)-terminated self-assembled monolayers investigated by frequency modulation atomic force microscopy in aqueous solution, *Nanotechnology*, 2014, **25**, 305602.

29 S. Zorn, N. Martin, A. Gerlach and F. Schreiber, Real-time PMIRRAS studies of in situ growth of C11Eg6OMe on gold and immersion effects, *Phys. Chem. Chem. Phys.*, 2010, **12**, 8985.

30 D. J. Vanderah, M. L. Walker, M. A. Rocco and K. A. Rubinson, Self-Assembled Monolayers of an Oligo (ethylene oxide) Disulfide and Its Corresponding Thiol Assembled from Water: Characterization and Protein Resistance, *Langmuir*, 2008, **24**, 826–829.

31 D. J. Vanderah, H. La, J. Naff, V. Silin and K. A. Rubinson, Control of Protein Adsorption: Molecular Level Structural and Spatial Variables, *J. Am. Chem. Soc.*, 2004, **126**, 13639–13641.

32 R. Valiokas, S. Svedhem, M. Östblom, S. C. T. Svensson and B. Liedberg, Influence of Specific Intermolecular Interactions on the Self-Assembly and Phase Behavior of Oligo(Ethylene Glycol)-Terminated Alkanethiolates on Gold, *J. Phys. Chem. B*, 2001, **105**, 5459–5469.

33 T. Miyazawa, K. Fukushima and Y. Ideguchi, Molecular Vibrations and Structure of High Polymers. III. Polarized Infrared Spectra, Normal Vibrations, and Helical Conformation of Polyethylene Glycol, *J. Chem. Phys.*, 1962, **37**, 2764–2776.

34 H. Matsuura and T. Miyazawa, Vibrational analysis of molten poly(ethylene glycol), *J. Polym. Sci., Part A-2*, 1969, **7**, 1735–1744.

35 L. Malysheva, Y. Klymenko, A. Onipko, R. Valiokas and B. Liedberg, Ab initio calculations of equilibrium geometries and vibrational excitations of helical ethylene-glycol oligomers: application to modeling of monolayer infrared spectra, *Chem. Phys. Lett.*, 2003, **370**, 451–459.

36 L. Malysheva, A. Onipko and B. Liedberg, Ab Initio Modeling of Defect Signatures in Infrared Reflection-Absorption Spectra of SAMs Exposing Methyl- and Hydrogen-Terminated Oligo(ethylene glycols), *J. Phys. Chem. A*, 2008, **112**, 728–736.

37 P. E. Laibinis, G. M. Whitesides, D. L. Allara, Y. T. Tao, A. N. Parikh and R. G. Nuzzo, Comparison of the structures and wetting properties of self-assembled monolayers of n-alkanethiols on the coinage metal surfaces, copper, silver, and gold, *J. Am. Chem. Soc.*, 1991, **113**, 7152–7167.

38 R. Valiokas, M. Östblom, S. Svedhem, S. C. T. Svensson and B. Liedberg, Temperature-Driven Phase Transitions in Oligo(ethylene glycol)-terminated Self-Assembled Monolayers, *J. Phys. Chem. B*, 2000, **104**, 7565–7569.

39 F. Schreiber, Structure and growth of self-assembling monolayers, *Prog. Surf. Sci.*, 2000, **65**, 151–257.

40 C. Vericat, M. E. Vela, G. Benitez, P. Carro and R. C. Salvarezza, Self-assembled monolayers of thiols and dithiols on gold: new challenges for a well-known system, *Chem. Soc. Rev.*, 2010, **39**, 1805.

41 J. Zheng, L. Li, S. Chen and S. Jiang, Molecular Simulation Study of Water Interactions with Oligo (Ethylene Glycol)-Terminated Alkanethiol Self-Assembled Monolayers, *Langmuir*, 2004, **20**, 8931–8938.

42 A. L. Sumner, E. J. Menke, Y. Dubowski, J. T. Newberg, R. M. Penner, J. C. Hemminger, L. M. Wingen, T. Brauers and

B. J. Finlayson-Pitts, The nature of water on surfaces of laboratory systems and implications for heterogeneous chemistry in the troposphere, *Phys. Chem. Chem. Phys.*, 2004, **6**, 604.

43 M. James, T. A. Darwish, S. Ciampi, S. O. Sylvester, Z. Zhang, A. Ng, J. J. Gooding and T. L. Hanley, Nanoscale condensation of water on self-assembled monolayers, *Soft Matter*, 2011, **7**, 5309.

44 S. G. Moussa, T. M. McIntire, M. Szőri, M. Roeselová, D. J. Tobias, R. L. Grimm, J. C. Hemminger and B. J. Finlayson-Pitts, Experimental and Theoretical Characterization of Adsorbed Water on Self-Assembled Monolayers: Understanding the Interaction of Water with Atmospherically Relevant Surfaces, *J. Phys. Chem. A*, 2009, **113**, 2060–2069.

45 K. Xu, P. Cao and J. R. Heath, Graphene Visualizes the First Water Adlayers on Mica at Ambient Conditions, *Science*, 2010, **329**, 1188–1191.

46 Y. Maréchal, The molecular structure of liquid water delivered by absorption spectroscopy in the whole IR region completed with thermodynamics data, *J. Mol. Struct.*, 2011, **1004**, 146–155.

47 K. Ramasesha, L. De Marco, A. Mandal and A. Tokmakoff, Water vibrations have strongly mixed intra- and intermolecular character, *Nat. Chem.*, 2013, **5**, 935–940.

48 B. M. Auer and J. L. Skinner, IR and Raman spectra of liquid water: Theory and interpretation, *J. Chem. Phys.*, 2008, **128**, 224511.

49 N. Kitadai, T. Sawai, R. Tonoue, S. Nakashima, M. Katsura and K. Fukushi, Effects of Ions on the OH Stretching Band of Water as Revealed by ATR-IR Spectroscopy, *J. Solution Chem.*, 2014, **43**, 1055–1077.

50 J.-J. Max and C. Chapados, Isotope effects in liquid water by infrared spectroscopy. III. H_2O and D_2O spectra from 6000 to cm−1, *J. Chem. Phys.*, 2009, **131**, 184505.